Journal of Materials Science: Composites

RESEARCH Open Access

Agriculture waste derived biochar based polyvinyl alcohol composites for structural applications

Kunal Joshi[1], Tanuja Arya[1], Neelam Rawat[1], Kundan Singh Rawat[1], Rajkumari Linthoinganbi[2,3], Pushpa Bhakuni Negi[4], Chetna Tewari[5*], Yong Chae Jung[5*] and Nanda Gopal Sahoo[1*]

Abstract

The sustainable development of high-performance materials from renewable resources has gained substantial attention in recent years. In this study, biochar was synthesized from agricultural waste i.e. bamboo waste (WBB) via a green route and subsequently functionalized with ammonium persulfate (APS) to improve dispersion and interfacial bonding. The functionalized bamboo waste biochar was incorporated into a polyvinyl alcohol (PVA) matrix to fabricate nanocomposites with enhanced structural properties. Comprehensive characterization was carried out using FTIR, XRD, FE-SEM, XPS, and Raman spectroscopy to confirm successful functionalization and uniform distribution of WBB within the PVA matrix. Mechanical testing revealed significant improvements in tensile strength, Young's modulus, and toughness, demonstrating the reinforcing effect of APS-functionalized waste bamboo biochar (WBFB). Thermal stability analysis confirmed enhanced resistance to degradation, further validating the material's suitability for engineering applications. The results revealed that the incorporation of WBFB significantly enhanced the performance of PVA. At an optimal biochar loading of 5 wt%, tensile strength increased by approximately 62.43% compared to pure PVA and Young's modulus increased from 3088 MPa (pure PVA) to 7496 MPa, respectively. Thermal stability also increased from 325.70 °C ($T_{50\%}$) for pure PVA to 384.81 °C ($T_{50\%}$) for the 5% biochar functionalized composite. DSC analysis revealed enhancement in the thermal characteristics T_m and T_c by 8.79 °C and 13.02 °C at an optimal biochar loading of 5 wt%. The synergistic combination of bamboo waste derived biochar and PVA establishes a cost-effective, eco-friendly, and mechanically robust nanocomposite with strong potential for use in advanced structural and sustainable material applications.

Keywords Agricultural waste, Polyvinyl alcohol, Biochar, Composite, Thermal stability, Mechanical properties

*Correspondence:
Chetna Tewari
chetna.tewari@kist.re.kr
Yong Chae Jung
ycjung@kist.re.kr
Nanda Gopal Sahoo
ngsahoo@yahoo.co.in
[1]Prof. Rajendra Singh Nanoscience and Nanotechnology Centre, Department of Chemistry, D.S.B. Campus, Kumaun University Nainital, Nainital, Uttarakhand, India
[2]Department of Nano Convergence Engineering, Jeonbuk National University, 567 Baekje-Daero, Jeonju 54896, Republic of Korea
[3]Institute of Advanced Composite Materials, Korea Institute of Science and Technology, 92 Chudong-ro, Bongdong-eup, Wanju-gun, Jeonbuk 55324, Republic of Korea
[4]Department of Chemistry, Graphic Era Hill University, Bhimtal Campus, Nainital, Uttarakhand, India
[5]RAMP Convergence Research Center, Korea Institute of Science and Technology (KIST), 92 Chudong-ro, Bongdong-eup, Wanju-gun, Jeonbuk 55324, Republic of Korea

Introduction

In today's environment, researchers are working to develop new environmentally friendly materials and technologies that improve product sustainability in response to growing global ecological consciousness and socioeconomic challenges [1]. Carbon has long been used as a filler to modify the characteristics of polymers. Carbon nanotubes (CNTs), graphene, activated carbon, biochar are now widely used as fillers in polymer composites due to their superior tensile, thermal, and electrical properties.

Biochar manufacturing has become a popular topic due to the abundance feedstock accessible, low cost, and good adsorption performance [2]. Biochar can be produced from a variety of agricultural wastes, including forest weed *Prosopis juliflora* [3], palm empty bunch litter [4], rice husk [5] and pinecones [6]. These feedstocks produce low-cost biochar while also adding value to agricultural waste. The quality of biochar is determined by the feedstock's physicochemical qualities and manufacturing procedure [7].

Drepanostachyum falcatum, often known as Himalayan weeping bamboo, is often classified grass or agricultural waste in the Himalayan region. Despite its high potassium content and limited usage in biomedical applications, research has focused on its potential as a low-cost adsorbent feedstock [8]. Among these renewable resources, bamboo waste is unique due to its availability, renewability, and potential to serve as a raw material for valuable products. As bamboo has cellulose concentration of 40% to 65%, which is extremely high when compared to other biomass waste, it has the potential to be utilized as a resource [9]. According to earlier studies, bamboo waste can be transformed into biochar using a number of methods, including acid treatment, microwave heating and microwave-assisted catalytic graphitization [10]. However, creating more ecologically acceptable substitute techniques remains a top focus in the on-going and sustainable development of biochar materials. The potential for biomass-derived biochar to exhibit properties akin to those of pure carbon-based material makes them appealing candidates for a range of applications [9–11].

Nowadays, a range of nontoxic and biodegradable polymer kinds have been employed in the creation of ecological appropriate materials for packaging, polymeric structural composite, textile structural composite and structural applications [12–15]. PVA is a biodegradable polymer with certain characteristics, including water solubility and multiple active OH groups [16]. PVA polymer has been widely utilized in packaging applications recently due to its good film-forming activity, high water solubility, non-toxicity, and superior oxygen barrier qualities [17]. Despite this, PVA has a number of limitations that limit its use in a variety of applications, including as poor water barrier qualities, high production costs, and limited dimensional stability, particularly in packaging materials [18–19]. In this field, the mechanical and thermal properties of materials are essential. The physical properties of such composites could be improved by the addition of fillers like biochar, graphene, carbon nanofiber (CNF), carbon nanotube (CNT), and graphene oxide (GO) [20–23]. The addition of biochar improves the thermal stability of polymer composites due to the nitrogen and oxygen containing functional groups on its surface. It also enhances the physical adsorption capability of polymer composites by increasing molecular interactions like hydrogen bonding [24].

Bamboo waste derived biochar has unique physical and chemical features that make it an important material for environmental applications. It has a high surface area, a microporous structure, and is lightweight, all of which increase its adsorption capability. Bamboo biochar is rich in carbon, has a stable aromatic structure, and frequently has a high cation exchange capacity (CEC). It has a slightly alkaline pH because of the presence of ash and minerals such as potassium, calcium, and magnesium. Bamboo biochar's composition and qualities can change based on pyrolysis circumstances including temperature, heating rate, and feedstock type, influencing its usefulness in applications like soil amendment, pollutant removal, and carbon sequestration Bamboo biochar typically has a surface area of 200 to 700 m^2/g, with a porosity (pore volume) of 0.2 to 1.5 cm^3/g [25–26].

Mousa et al. [27] demonstrated that eco-friendly PVA/bamboo charcoal (BC) nanocomposite films can be made efficiently using a simple solution casting approach, resulting in good BC dispersibility within the polymer matrix. The incorporation of 3 wt% BC resulted in significant increases in mechanical performance, with tensile modulus increasing by 70.2% and tensile strength increasing by 71.6% compared to neat PVA. The nanocomposites also demonstrated improved thermal stability, as evidenced by a 17.8% increase in decomposition temperature at 80% weight loss. These findings suggest that BCs are a sustainable, low-toxicity alternative to traditional carbon-based nanofillers, with high potential for use in environmentally friendly thin-film packaging materials. According to Sahoo et al. [28] study into the effects of GO and PVA functionalized GO on PVA nanocomposites, adding 1 wt% functionalized GO resulted in an astounding 88% increase in tensile strength and a 150% rise in Young's modulus. Nan et al. [29] observed that the addition of biochar reduced the ductility of PVA. However, they noticed a rise in the tensile modulus, a measure of polymer toughness, due to biochar's inherently higher rigidity than PVA. While a number of studies have reported enhanced mechanical and thermal

properties of PVA composites using biochar [27–29] issues with controlled functionalization, interfacial compatibility, uniform filler dispersion, and the simultaneous improvement of mechanical and thermal properties using environmentally friendly techniques still exist. Although the fact that bamboo biochar has been studied as filler in PVA composites, systematic research on chemically functionalized bamboo biochar made ecologically and its impact on structure property relationships in PVA nanocomposites is limited. In particular the function of ammonium persulfate based functionalization in improving the dispersion, interfacial hydrogen bonding, and multifunctional performance of bamboo biochar/PVA systems has not received enough attention. Furthermore, limited attention has been given to utilizing Himalayan bamboo waste as a sustainable carbon source for high-performance polymer nanocomposites.

In this context, we have created more environmentally friendly, cost-effective, and natural methods for synthesizing biochar and its analogues, which have attracted a lot of attention. Researchers have investigated and used a number of methods to create enormous amounts of biochar [8]. Biochar is synthesized using waste bamboo as a precursor material in our self-designed machine, 'SWAYAMBHU-WRM 2021' as reported in the literature by our research group [30]. This research takes a unique approach by utilizing waste bamboo as a precursor material for biochar production, contributing to waste reduction, cost effectiveness and promoting recycling efforts. Also by incorporating functionalized biochar within the PVA polymer matrix, the resulting composite material can exhibit enhanced tensile strength, modulus, and toughness compared to pure PVA. Incorporating waste bamboo derived biochar into PVA not only enhances the mechanical properties of the polymer but also contributes to waste utilization and recycling efforts. Using distilled water as the solvent, we synthesized PVA/WBFB nanocomposites for varying weight percentages (wt%) of WBFB in an easy, eco-friendly procedure. The miscibility of WBFB was investigated by structural research. Due to this characteristic of WBFB, the nanofiller can be distributed evenly throughout the PVA matrix without clumping together, resulting in homogeneous films and improved thermal characteristics. The morphological, mechanical, and thermal characteristics of the nanocomposites were examined, along with their molecular interactions. This innovative method not only contributes to the sustainable management of waste bamboo but also enhances the properties of the resulting composite, making it suitable for various applications. Our study underscores the potential of waste bamboo upcycling in advancing materials science towards environmentally friendly solutions.

Materials and methods

Chemicals and reagents

Bamboo stem (*Drepanostachyum falcatum*) was collected from the local forest of the Nainital region (Uttarakhand, India) 29.3924°N, 79.4534°E. Ethanol, Double distilled water (DDW), Ammonium persulfate (APS), Hydrochloric acid (HCl), Ethanol, Poly vinyl alcohol (PVA) pellets (99% purity, molecular weight approximately 1,15,000) were acquired from the LOBA Chemie Pvt.Ltd., Colaba Mumbai India.

Synthesis of biochar from bamboo waste

The *D.falcatum* plant was collected at Nainital, India, located in the Himalayan region. In order to get rid of dust and other contaminants, the plant's stem was first detached from its leaves and cleaned with tap water. After that, the stem was chopped into smaller pieces (about 1 inch), placed in a closed flask with a 1:1 ethanol and DDW water combination, and shaken constantly for 24 h in a rotary shaker. After grinding the mixture in a mixer, the plant's fiber and extract were separated by squeezing the mixture to create a paste. After being squeezed, the fiber was left in a hot air oven for the whole night to eliminate any remaining solvent or water content and prevent gas formation during pyrolysis. Then, 100 g of dry fiber was heated at a rate of 5 °C per minute to 400 °C for slow pyrolysis in an inert atmosphere of N_2 gas (20 ml/min) in a pyrolysis chamber. As a result, the black, charred residue was ground into a powder in a ball mill and then added to the secondary reactor at 600 °C with an inert atmosphere of N_2 gas (20 ml/min) and a heating rate of 10 C/min. The resulting black residue was completely cleaned with acidic water (5% HCl), and then it was repeatedly rinsed with DDW until the pH of the wash water was neutral (~7). Following an overnight drying process at 90 °C in an oven, it was ground in a mortar and pestle to create WBB a powdered form of Bamboo. Figure 1 shows the Synthesis route of Waste Bamboo Biochar (WBB).

Functionalization of WBB using APS

The APS functionalized WBB was prepared by a hydrothermal route as shown in Fig. 2 using APS as the precursor. In a typical preparation method, APS and WBB dispersions (~10 mg/mL) were combined with distinguishable weight combinations (1:1) and shifted into Teflon-lined auto clave containing 70 mL capacity, and hydrothermal reaction was performed at 200 °C for 24 h. Finally, the obtained precipitate was centrifuged and washed with hot water and ethanol accompanied by subsequent drying at 60 °C overnight in an oven and named as Waste Bamboo Functionalized Biochar (WBFB).

Fig. 1 Synthesis route of Waste Bamboo Biochar (WBB)

Preparation of WBFB/PVA nanocomposites

WBFB/PVA nanocomposite films containing WBFB nanofiller were prepared by dissolving 2 g of PVA polymer flakes in 40 mL of DDW constant stirring under for 2 h. The following process, which was carried out in a water bath with a nominal heat of 60 °C for 12 h a crystal-clear PVA solution was then obtained. Using magnetic stirring, a predetermined amount of WBFB was thoroughly mixed with 10 ml of DDW for one hour. We prepared a variety of PVA composite films with 0.2, 0.5, 1, 3, and 5 wt% of WBFB in relation to PVA in order to examine the impact of the amount of WBFB in the polymer matrix.

The composite film was synthesised by first dissolving the PVA fully with DDW followed by the brownish colour WBFB solution accumulation. The resultant mixture was agitated to create a uniform WBFB/PVA nanocomposite solution for 12 h under constant stirring. After that, the homogeneous solution was slowly poured into a borosilicate glass petri dish and heated in a vacuum oven for 12 h at 60 °C. For testing, the fully desiccated films were scraped from the plate. WBFB/PVA films with different WBFB weight percentages were prepared using a similar method.

Characterization

FT-IR spectra were analyzed with an average of 16 scans, covering wavenumbers from approximately 400 and 4000 cm^{-1}. Using the ATR technique, this analysis was carried out using a PerkinElmer Instrument (model: Spectrum Two). The functional groups and interactions between WBFB and the PVA matrix were determined using the FT-IR technique. A high-resolution X-ray diffractometer (Rigaku Smart Lab) equipped with Cu-Kα radiation (wavelength of 0.154 nm) was used to perform X-ray diffraction (XRD) spectroscopy in order to assess the crystalline/amorphous structure of WBB. Operating parameters were adjusted to 45 kV and 200 mA, and data was gathered at a rate of 4°/min within a scanning range of 10°–80°.Raman spectroscopy (Horiba Japan Xplora Plus, 514 nm) was performed to analyze the structure and properties of WBB. Tests of the PVA composite films' tensile strength were conducted using an Instron 5967 at room temperature, with a gauge length of 10 mm and a loading rate of 5 mm/min. A TGA-PerkinElmer

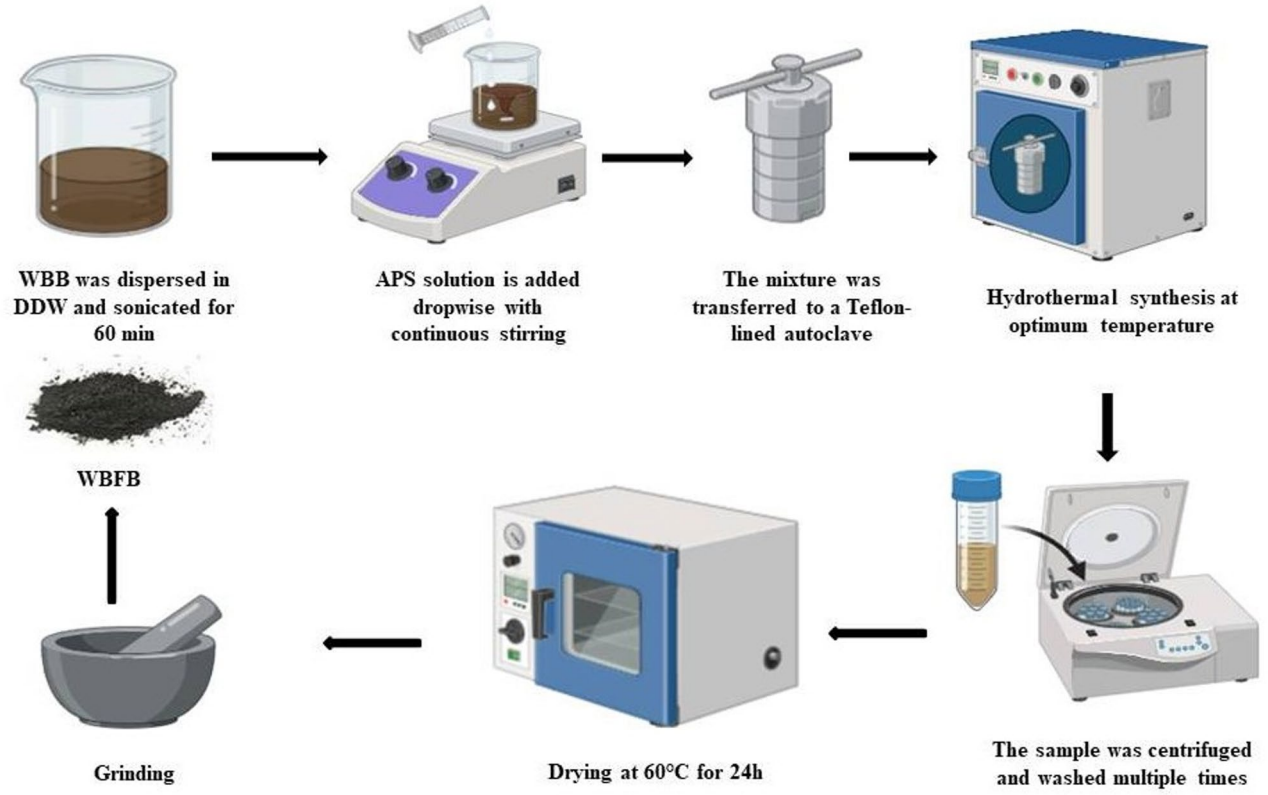

Fig. 2 Synthesis route of functionalization of Waste Bamboo Biochar (WBFB)

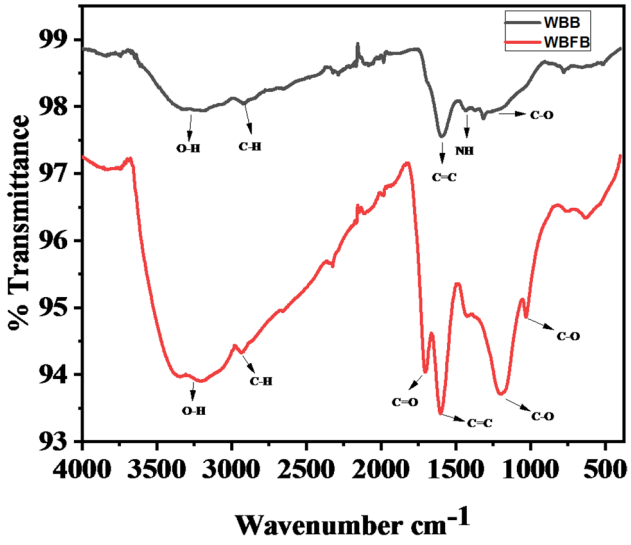

Fig. 3 FT-IR of WBB and WBFB

4000 thermal analyzer was used to assess the WBFB and PVA nanocomposites thermal stability. The samples were subjected to TGA in a nitrogen environment at temperatures ranging from 30 to 800 °C, with a flow rate of 10 °C per minute and a gas flow of 19.8 mL/min. Using a PerkinElmer DSC 4000, thermal properties (T_m and T_c) were displayed. First, the samples were heated through a cycle, and then they were cooled under identical conditions. All runs involved heating the samples from 30 to 250 °C, holding them there for one minute, and then cooling them down at a rate of 10 °C per minute from 250 to 30 °C. The N_2 flow was maintained at 19.8 mL/min while about 5 mg of the sample was put in an aluminium pan.

Result and discussion

Characterization of synthesized WBB and WBFB

The FT-IR spectra were analyzed to determine the different functional groups present on the WBB and WBFB surface that are displayed in Fig. 3. The broad peak at around 3328.93 cm^{-1} was attributed to O-H stretching from the hydroxyl group on the surface. Aliphatic C-H groups are present, as indicated by the low intensity peaks at about 2921.44 cm^{-1}.The peaks at about 1609.98 cm^{-1} verified that an aromatic C = C group was present. The strong band located at around 1436.49 cm^{-1} is ascribed to N-H bending vibration. The band at about 1280 cm^{-1} is an aromatic C-O stretching band. The OH and phenolic OH groups C-O stretching vibration is the cause of the band at about 1316 cm^{-1} [31]. Similar to WBFB, epoxy functionality and C-O stretching vibrations were observed at 1030.58 cm^{-1} and 1199.81 cm^{-1}, respectively. The hydroxyl groups (O-H) and carbonyl groups (C = O) both vibrated at 3210.20 cm^{-1} and

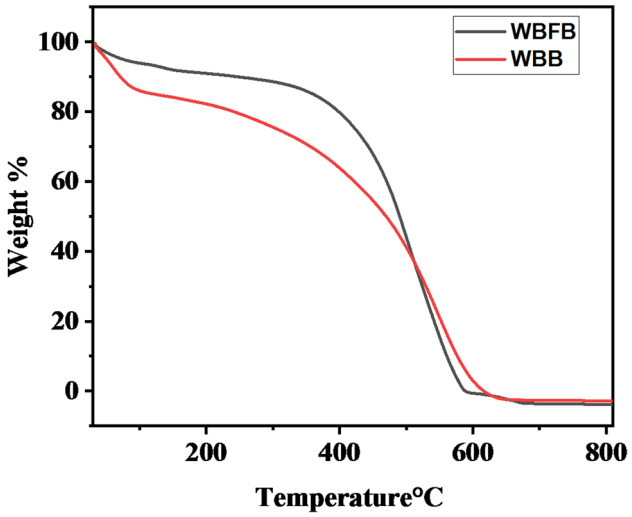

Fig. 4 TGA analysis of WBB and WBFB

Table 1 TGA data for WBB and WBFB

Sample composition	$T_{10\%}$ (°C)	$T_{15\%}$ (°C)	$T_{50\%}$ (°C)
WBB	70.97	122.25	469.36
WBFB	245.2	360.6	490.09

1701.83 cm^{-1}, respectively, indicating a significant degree of oxygenated functionality in WBFB. There are also aliphatic C-H groups, as seen by the low intensity peaks at roughly 2936.67 cm^{-1}, the C-O stretching, and the C = C stretching at 1603.01 cm^{-1} [32].

TGA was used to analyze the thermal properties of WBB and WBFB at temperatures between 30 and 800 °C as illustrated in Fig. 4. Both materials exhibit an initial weight loss below 150 °C, which can be attributed to the evaporation of physically adsorbed moisture and volatile components. In the temperature range of approximately 150 °C to 500 °C, a major weight loss is observed in both samples, corresponding to the decomposition of labile oxygen-containing functional groups such as hydroxyl, carboxyl, and epoxy groups [8]. WBFB degrade slowly and at slow rate due to functionalization which increases thermal stabilization to WBB. Above 500 °C, WBFB retained a slightly higher residual mass compared to WBB. Thermal stability increased from 469.36 °C ($T_{50\%}$) for WBB to 490.09 °C ($T_{50\%}$) for the WBFB.The WBFB demonstrates greater thermal stability than WBB as shown in Table 1, likely due to stronger interlayer interactions, reduced defect density, and improved graphitization resulting from APS functionalization.

The X-ray diffraction study enables us to have detailed information in terms of the structural changes that ammonium persulfate (APS) functionalization of the waste bamboo undergoes. The comparative analysis shows that there is a substantial increase in crystallinity and new ordered phases are formed after chemical functionalization.

The XRDs of both WBFB and WBB as shown in Fig. 5, indicate evident differences in crystallinity and phase composition which can be ascribed to the properties of functionalization and precursor. WBFB has a pattern of

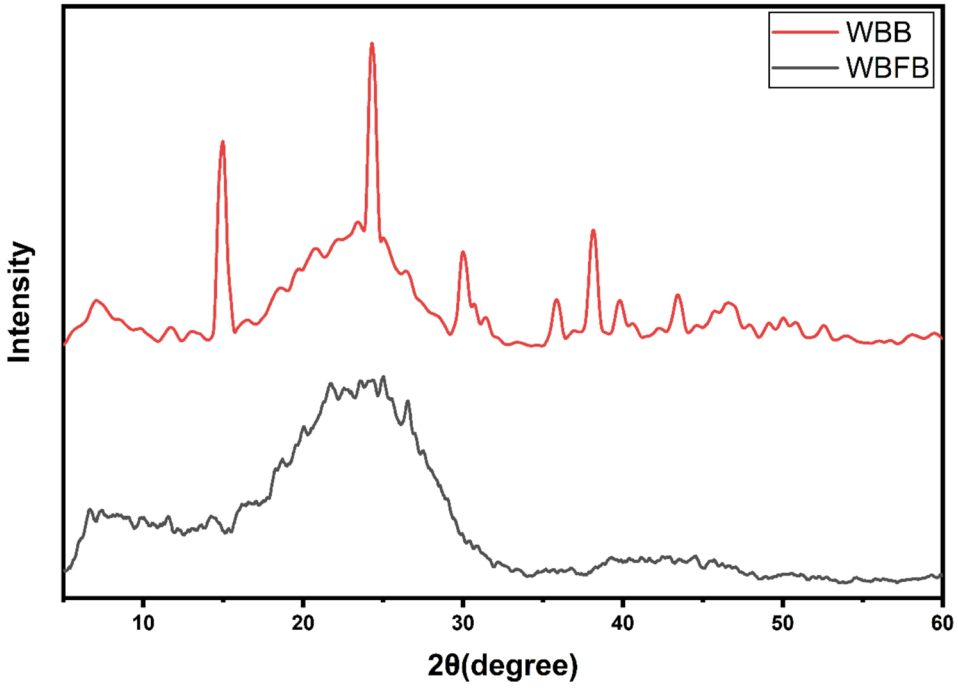

Fig. 5 XRD pattern of WBB and WBFB

steep peaks on its 2θ at values of 15°, 24°, 30.0°, 35.7°, 38.1°, 39.8° and 43.4°. The presence of these peaks is characteristic of crystalline inorganic phases together with partially ordered carbon domains caused during functionalization. The 24° and 43°-46° peaks can be attributed to the (002) and (100/101) planes of turbostratic or graphitic carbon respectively that suggest partial graphitization and progressive arrangement of the layers of aromatic carbon. The presence of sharp reflections in the intermediate 30°-39° indicates that the mineral phases or left-over salts, might be present, which are typically observed in biochar following chemical treatment [33–34].

Conversely, WBB has very broad peaks that are concentrated around an approximate of 7.7° and 23.7° which indicates its largely amorphous character with little graphitization. The wide peak at about 23° is characteristic of chaotic carbon matrices (002 plane), and no other sharp peaks imply that there are no major crystalline phases and that stacking of carbon layers is not complete. These characteristics are typical of biochar pyrolysed at moderate temperatures, which contains a greater percentage of amorphous carbon [34–35].

In WBB, the (002) peak at 2θ of 23° with the crystallite size of 0.85 nm representing a disordered graphitic structure that has an expanded interlayer spacing characteristic [36–37]. WBFB's (002) peak after APS functionalization moves to 24.5° with a shorter d_{002} spacing of 3.64 nm, and grows in size with 1.31 nm crystallites [38]. This 0.016 nm decrease in interlayer spacing causes the material to move nearer to pure graphite, which indicates a greater π-π stacking and a higher graphitic order [39].

The value indicates that the full-width half maxima (FWHM) obtained in WBB is reduced significantly in WBFB, showing much better long-range crystalline order [40]. The crystallite size improves by 54% as the crystallite size is improved to 1.31 nm. The mean crystallite size changes between 0.86 nm in WBB to 8.14 nm in WBFB which means significant domains growth and structural rearrangement. The WBFB pattern displays a number of other diffraction peaks not present in WBB, showing the existence of new ordered phases. 15° broad peak at 2θ, is probably related to the intermediate oxidation products developed during APS treatment.

The persulfate-based functionalization offers selective oxidation that does not cause damage to the lattice on a large scale and results in the introduction of functional groups at sites of defects and edges [41]. This biased strategy is the reason why WBFB shows better crystallinity. This characteristic of graphite retention with the attainment of improved functionality is an ideal ratio of structural integrity and reactivity on the surface [42]. The XRD comparison establishes that APS functionalization is a viable solution to developing the structural and functional properties of bamboo-derived biochar as an effective method of controlling material modification without modifying its graphitic nature and providing ample functionality on the surface.

Raman spectroscopy was used to examine the structure of waste bamboo biochar (WBB) and APS functionalized biochar (WBFB) as shown in Fig. 6. The samples exhibited both the D and G bands that are characteristic of carbon-based material. In the case of WBB, the D-band was noted at 1353 cm^{-1}, whereas the G-band was noted at 1572 cm^{-1} [43]. The D and G bands in WBFB were slightly shifted to 1356 cm^{-1} and 1583 cm^{-1} respectively. D-band means the existence of disordered carbon or structural defect, and the G-band is the in-plane vibration of sp^2-bonded carbon atoms of a graphitic lattice [44–47].

Also, both spectra had a band at around 2986 cm^{-1} (WBB) and 2992 cm^{-1} (WBFB) at the D + G band, the overtone of the D-band which gives data on stacking order and the thickness of the graphitic layers which is a product of one D-mode phonon and one G-mode phonon scattering. Second order Raman process, this band frequently represents extended graphitic domains that are somewhat disordered, as found in biochar and in part in graphitized carbons. [48–49]. This aspect is more pronounced in WBB and is weaker in WBFB, meaning that the hydrogenated sp^3 carbon environments are weakened during the N and S doping [50]. This reduced C-H envelope in WBFB is also in agreement with the substitutional incorporation of heteroatoms and dehydrogenation of the C-H sites at the edges to C-N or C-S and to graphitized domains, as indicated by the increased I_D/I_G ratio and the XPS evidence of the N and S functionalities.

The D/G ratio of intensity of the D and G bands (I_D/I_G) is the measure of the disorder of structures in the samples. The WBB, which was 2.11, had an I_D/I_G ratio that was way lower, whereas WBFB, which was 4.2, had a significantly higher I_D/I_G ratio. The increased I_D/I_G ratio of WBFB indicates that functionalization using APS created more defects or disorders to the graphitic structure of the biochar. This outcome is in line with earlier experiments, in which modification and doping (e.g., with persulfate or heteroatoms) in chemistry can lead to increased defect density, and thus, to a higher I_D/I_G ratio [44, 51, 52].

Therefore, the Raman analysis proves the effective functionalization of waste bamboo biochar because the shift in the positions of the peaks and the significant growth of the I_D/I_G ratio after the incubation with APS confirm the successful functionalization of waste bamboo biochar.

The surface morphology of WBFB and WBB was examined using FE-SEM analysis. The FE-SEM pictures of WBFB and WBB are shown in Fig. 7(a-d). Both the WBFB and the WBB showed a disordered surface

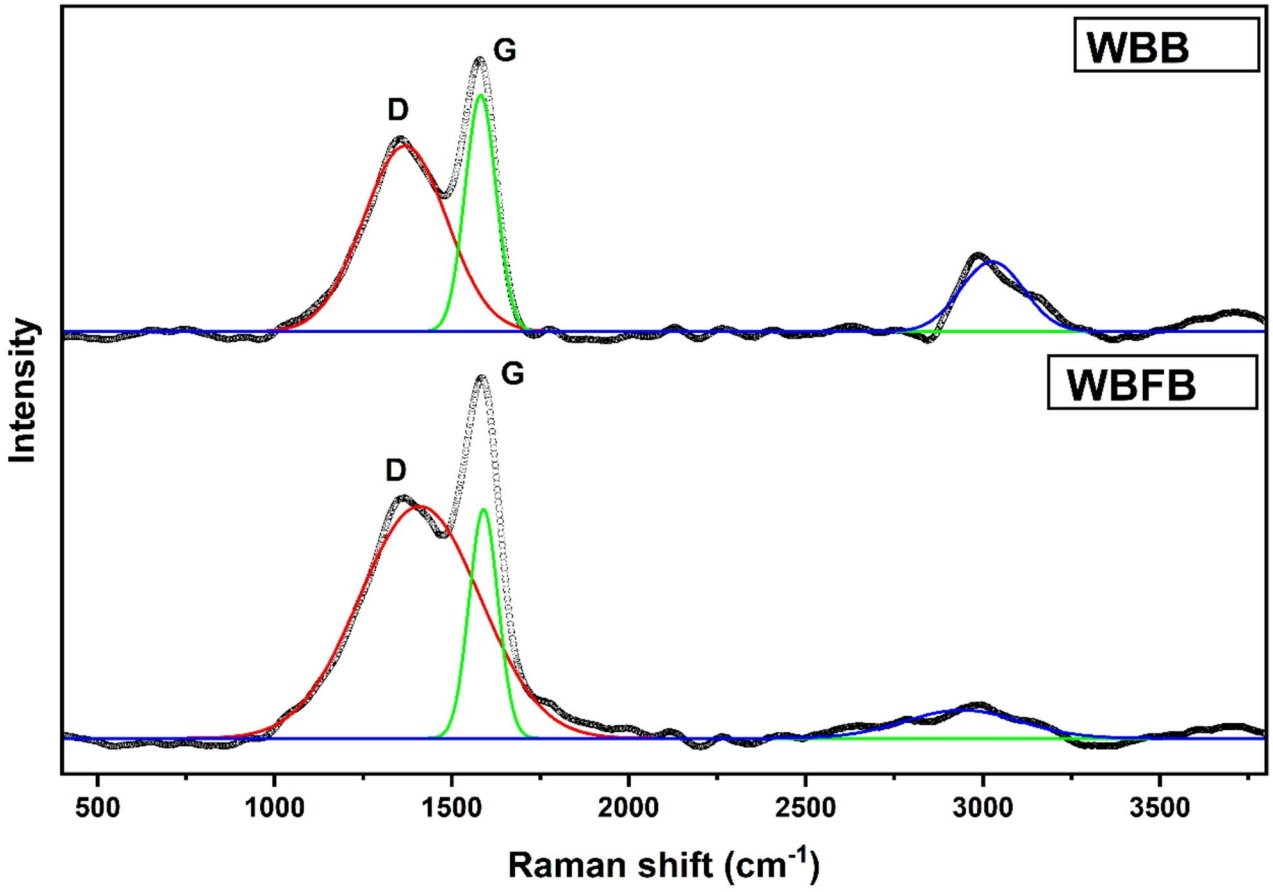

Fig. 6 Raman spectra of WBB and WBFB

structure consisting of different sized flakes like morphology and agglomerated nanoparticles (Fig. 7a-d). In short, a rough and porous nanostructure with a significant surface area is seen at lower magnifications (Fig. 7c). Additionally, these images demonstrate that the WBFB and WBB have a lengthy structure and contain irregularly shaped impurities [9]. Although the nanoparticles in (Fig. 7a-d) appear to be clustered together at lower magnification. The thicker disordered surface structure may be caused by oxygen-containing functions at the edges, above, and below the nanosheets. At increased magnification, a rough, porous nanostructure with a sizable surface area is displayed.

X-ray photoelectron spectroscopy (XPS) was conducted to examine the incorporation of heteroatoms and alterations in chemical bonding between the pristine waste bamboo biochar (WBB) and the APS-functionalized biochar (WBFB). The survey spectra (Fig. 8) distinctly reveal the presence of C_{1s} and O_{1s} peaks in both samples, whereas WBFB additionally displays notable N_{1s} and S_{2p}. Thereby confirming the effective introduction of nitrogen and sulfur functionalities during the functionalization process. The quantitative elemental composition derived from the survey spectra is presented in Table 2. WBB comprises 81.25 at% C and 18.75 at% O, which aligns with the characteristics of a typical high-carbon lignocellulosic biochar structure. Conversely, WBFB shows 72.58 at% C, 24.6 at% O, along with 1.92 at% N and 0.9 at% S, suggesting that the APS treatment facilitates the incorporation of heteroatoms and enhances the presence of oxygen-based functional groups. This outcome is anticipated, as persulfate oxidation is recognised for introducing -OH, -COOH, $-SO_4^{2-}$, and sulfonate/sulfone groups while partially disrupting the graphitic framework [53–54].

High-resolution XPS analysis offers a more profound understanding of the chemical environments found in both WBB and WBFB. In the WBB sample, the C_{1s} spectrum prominently features a significant sp^2/sp^3 carbon peak at 284.82 eV, which is indicative of aromatic ring structures and graphitic carbon commonly associated with lignocellulosic biochars. This is further complemented by a secondary component at 286.90 eV, which is attributed to C-O functionalities that originate from hydroxyl or ether groups retained from biomass precursors [55–56]. Following the treatment with persulfate,

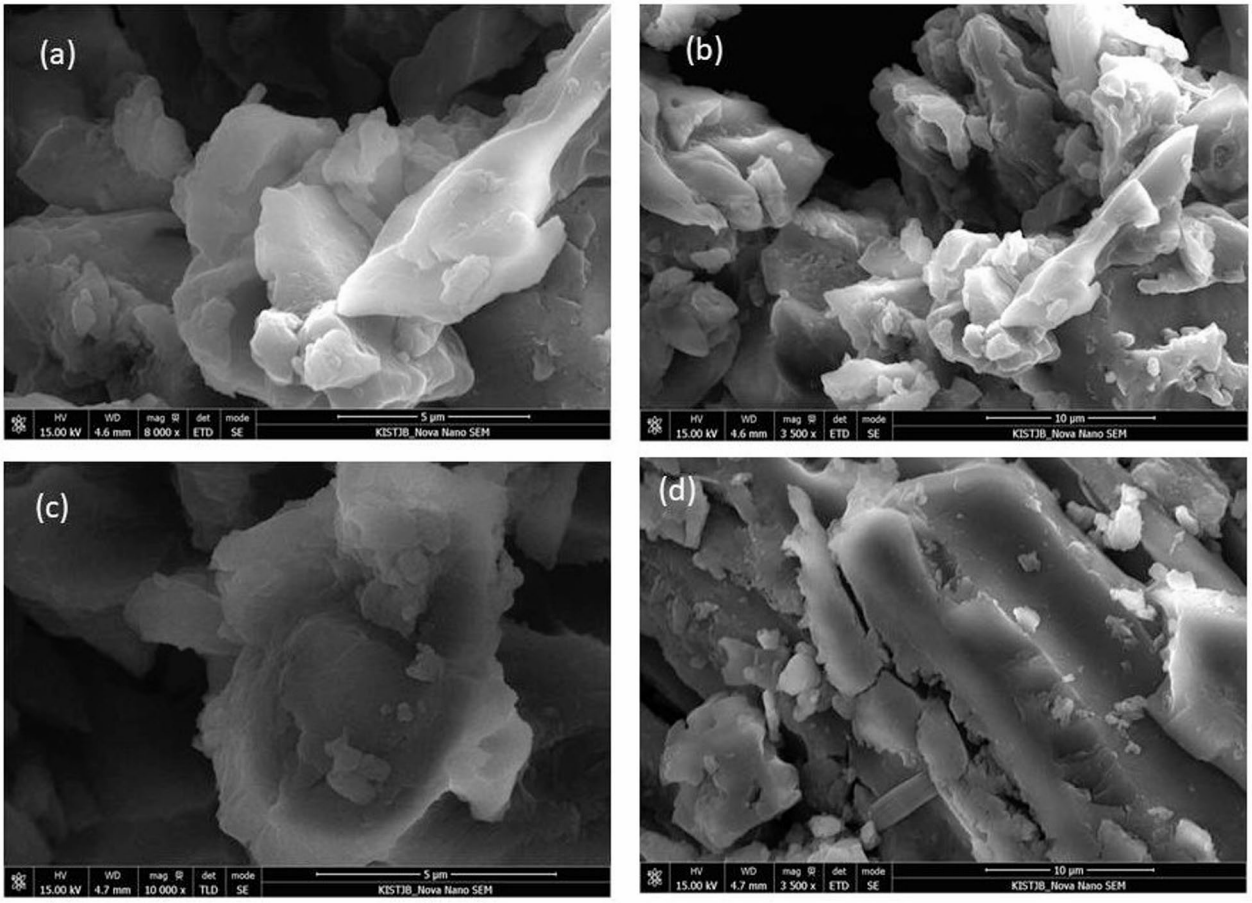

Fig. 7 FE-SEM analysis of (**a**, **b**) WBB and (**c**, **d**) WBFB

the WBFB C_{1s} envelope exhibits broadening and a shift, indicating significant chemical alterations. The primary carbon peak at 285.02 eV suggests a disturbed graphitic environment resulting from the addition of electron-withdrawing oxygen and sulfate groups. Additionally, the appearance of a more pronounced carbonyl-related component at 287.37 eV validates the creation of oxidized species such as C = O and O–C = O groups. The observed increases in carbonyl and oxygen-functional groups are characteristic of vigorous oxidative treatments, particularly those that involve sulfate radicals and persulfate activation, which lead to the introduction of defects and surface heteroatom sites [55–56]. The O_{1s} spectra further substantiate this oxidative transformation. WBB shows two distinct oxygen environments, a lower-binding-energy peak at 531.50 eV, which is attributed to carbonyl and quinone-type oxygen, and a higher-binding-energy peak at 533.06 eV, corresponding to C-O-C and phenolic oxygen groups typically found in biochars [55–56]. In contrast, WBFB presents a single, broader O_{1s} feature centred at 532.80 eV, reflecting a convolution of carbonyl, hydroxyl, and sulfate-derived oxygen atoms. This convergence into a predominant oxidised oxygen peak aligns with the incorporation of sulfate and sulfonate functionalities during persulfate activation, which modifies the oxygen environment on the carbon surface [56]. Nitrogen is only present following functionalization, and the WBFB, N_{1s} spectrum verifies successful nitrogen doping by revealing three chemically distinct nitrogen states. A peak at 400.8 eV is associated with pyrrolic or amide-type nitrogen integrated into the carbon matrix, whereas the peaks at 405.7 eV and 407.5 eV are indicative of highly oxidised nitrogen environments, such as nitrate-like or NO_x species. These nitrogen configurations are commonly found in carbons treated with ammonium persulfate, where oxidative cleavage and radical reactions incorporate nitrogen into edge sites or oxidised regions of the carbon structure [57–58]. The S_{2p} region of WBFB further confirms the incorporation of sulfur through a distinct doublet observed at 167.8 eV and 168.7 eV, which is characteristic of oxidised sulfur species such as sulfate (SO_4^{2-}) and sulfone groups. These binding energies align perfectly with the grafting derived from persulfate [59–60].

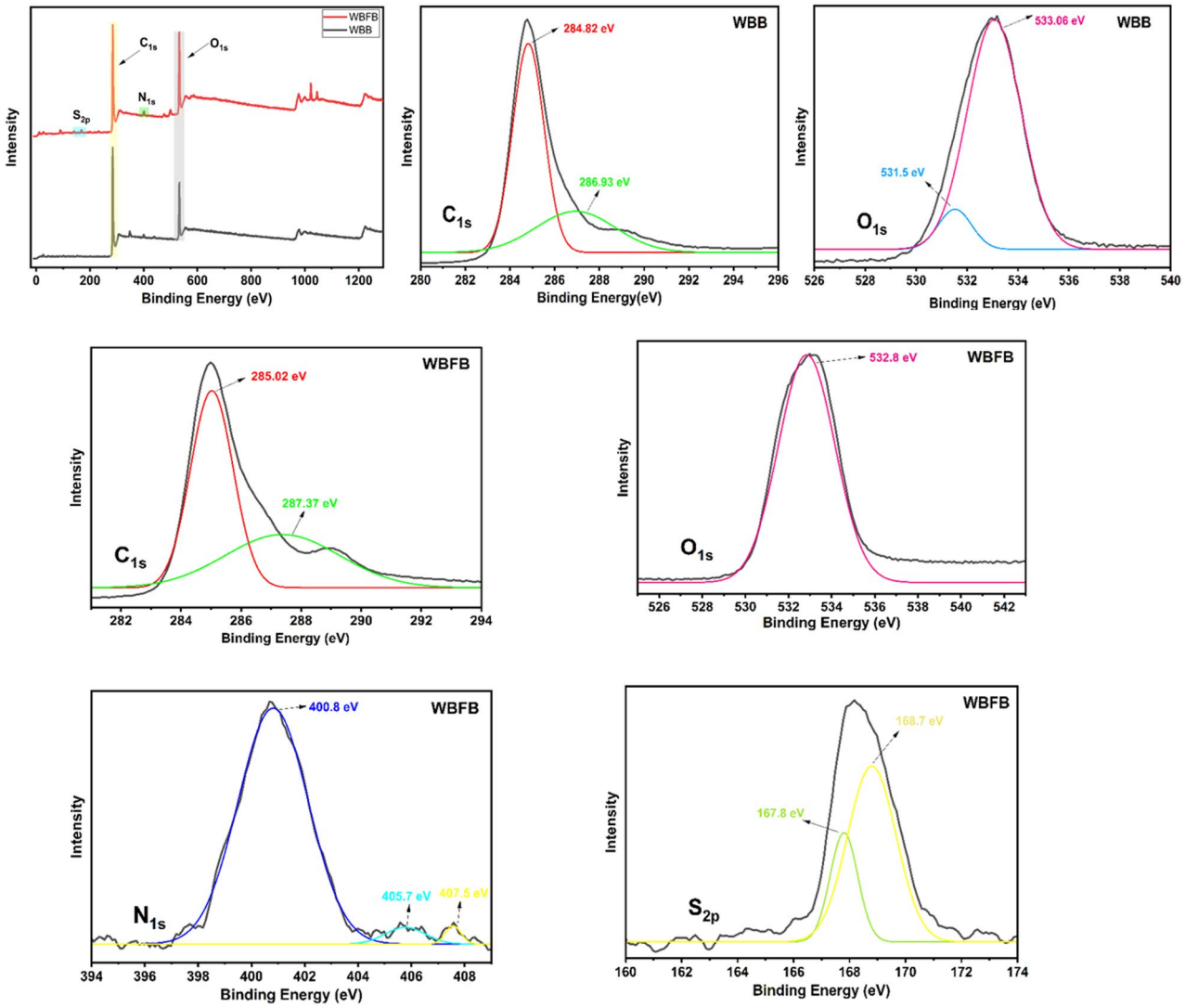

Fig. 8 XPS of WBB and WBFB

Table 2 XPS interpretation of WBB and WBFB

Sample	C_{1s} (at%)	O_{1s} (at%)	N_{1s} (at%)	S_{2p} (at%)
WBB	81.25	18.75	-	-
WBFB	72.58	24.6	1.92	0.9

WBFB dispersion in PVA and molecular interactions at the interface

To better understand the functional groups present in the synthesized sample, FT-IR spectroscopy was conducted as shown in Fig. 9. When molecules interact, the energy required for their vibrational modes can be altered, leading to shifts in peak positions within the FTIR spectrum. Well-dispersed nanofillers typically cause more distinct peak shifts compared to those that are aggregated or poorly dispersed. Notable changes in the spectra were observed with varying concentrations of WBFB nanofillers. The broad O–H stretching band shifted to a lower wavenumber, indicating the formation of stronger hydrogen bonds between the hydroxyl groups of PVA and the oxygen-containing functional groups (such as –OH, –COOH, and epoxy) present on WBFB [11]. This interaction was further evidenced by the broadening of the C–O–C and C–O stretching bands observed between 1092 and 1326 cm^{-1}. In the case of the 5 wt% WBFB/PVA composites, even more pronounced spectral changes were evident. The hydroxyl groups (O-H) vibrated at 3274 cm^{-1}. The distinct peak at 2915 cm^{-1} corresponds to asymmetric C–H stretching, while the 2848 cm^{-1} peak is attributed to symmetric C–H stretching. The vibration at 1472 cm^{-1} is linked to in-plane C–H bending, and the peak at 797 cm^{-1} is associated with the rocking vibrations of the $–CH_2–$ groups, reflecting the long polymer chains and high degree of polymerization in PVA. In the nanocomposite containing 5 wt% WBFB, slight shifts in the symmetric and asymmetric $–CH_2–$ stretching bands were noted, moving from 2919.15 to 2848 cm^{-1} in pure

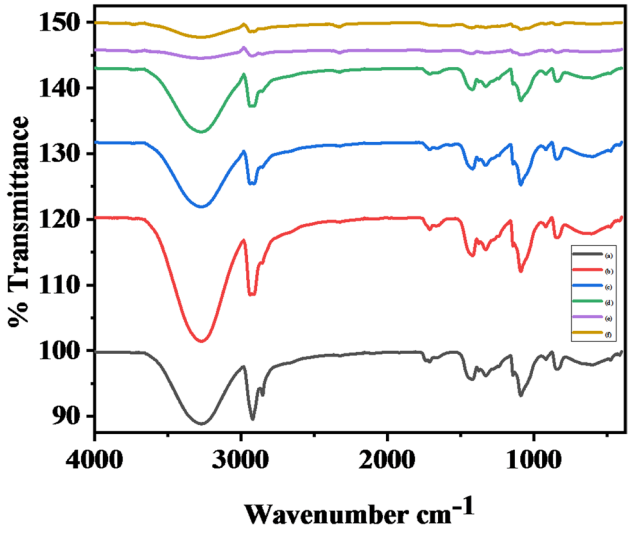

Fig. 9 FT-IR of (**a**) Pure PVA (**b**) 0.2% WBFB/PVA (**c**) 0.5% WBFB/PVA (**d**) 1.0% WBFB/PVA (**e**) 3.0% WBFB/PVA (**f**) 5.0% WBFB/PVA

PVA to 2919.92 and 2848.18 cm^{-1}, respectively. Additional bands were observed at 1740 cm^{-1} (C = O), 1541 cm^{-1} (S–H), and 1095 cm^{-1} (C–O–C) with the incorporation of 0.2, 0.5, 1, 3, and 5 wt% WBFB. These features confirm the uniform dispersion of WBFB within the PVA matrix and highlight its critical role in influencing molecular interactions in the composite. The observed peak shifts provide important insights into the type and degree of interactions between the polymer and filler materials.

Thermal properties of WBFB/PVA nanocomposites

The thermal stability of prepared PVA nanocomposite samples was also assessed using TGA, as shown in Fig. 10. The TGA measurements of pure PVA and 0.2wt % WBFB/PVA, 0.5wt% WBFB/PVA, 1wt% WBFB/PVA, 3wt% WBFB/PVA, and 5wt% WBFB/PVA nanocomposites were performed in an inert nitrogen atmosphere heated at the rate of 10 °C/min from 30 °C to 800 °C. The TGA indicates that all the WBFB/PVA nanocomposites went through two significant stages of thermal degradation behaviour. The first stage of thermal degradation occurred below 170 °C because of the removal of water molecules from the PVA nanocomposite. The second stage emerged between the temperature ranges of 255 °C and 380 °C, due to the degradation of the pure PVA [61]. Thermal weight losses of 10%, 15%, and 50% have been taken into consideration to demonstrate the thermal stability of the WBFB/PVA polymer nanocomposites (Table 3). The thermal decomposition temperatures for the 10%, 15%, and 50% of pure PVA polymer were found to be 276.17 °C, 286.67 °C, and 325.70 °C, respectively. The $T_{10\%}$, $T_{15\%}$, and $T_{50\%}$ values can be further increased by incorporating 0.2, 0.5, 1, 3, and 5 wt% amounts of WBFB into the PVA matrix. Thus, for the 5 wt% WBFB/PVA nanocomposite, $T_{10\%}$, $T_{15\%}$, and $T_{50\%}$values were increased by 284.89 °C, 317.55 °C, and 384.81 °C, respectively, which are slightly higher than those of pure PVA. Due to the optimized intermolecular H-bonding interactions between the PVA matrix and the WBFB, the degradation temperatures of the nanocomposites have exhibited a moderate shift to a higher range in comparison with the pure PVA matrix [62–63]. Due to WBFBs high thermal stability, which improves heat dissipation inside the polymer matrix, the incorporation of WBFB effectively improved the thermal stability of the PVA polymer. The homogeneous distribution and robust interfacial interaction of WBFB and PVA polymer result in an improvement in thermal stability, which slows the thermal decomposition of the polymer nanocomposites.

The DSC analyses of various WBFB/PVA nanocomposites are depicted in Fig. 11. DSC analysis was carried out for each PVA nanocomposite film to ascertain the values of T_m and T_c for the nanocomposites and to ascertain the extent to which the addition of WBFB impacted the thermal transitions of PVA. When WBFB is incorporated to the PVA matrix, it disperses well, causing the WBFB nanoparticles to act as nucleating agents, supporting the material's crystalline nature and raising the crystallization peak temperature [64]. The T_m and T_c of WBFB/PVA nanocomposites and pure PVA, as determined by DSC analysis, are displayed in Table 4. As the amount of WBFB in the PVA matrix increases, so do the observed values for T_m and T_c. The T_m of PVA composites containing 5 wt% WBFB was 223.32 °C, while the T_m of pure PVA polymer was 214.53 °C. According to FT-IR research, this improvement is caused by the substantial H-bonding contact between the WBFB nanoparticles and the PVA polymer interface as well as the even distribution and dispersion of WBFB nanoparticles throughout the PVA matrix [12]. According to the samples' most recent cooling measurement, pure PVA's T_c was found to be 122.25 °C. The T_c shifts towards a higher temperature 135.27 °C for 5 wt% WBFB. When WBFB nanosheets are added to the PVA polymer 13.02 °C are the T_c enhancements for the PVA composites with 5 wt%.T_c values grow as a result of the heterogeneous nucleation impact of WBFB in the polymer matrix, which is essential for the crystallization of the PVA during the cooling run.

Mechanical behaviour of PVA/WBFB nanocomposites

Tensile tests were performed to ascertain how the inclusion of the filler impacts the PVA polymer's and its nanocomposites' mechanical strength. It was anticipated that the strong interfacial adhesion caused by H-bonding between the biochar and the PVA matrix, the high aspect ratio of the biochar, and the molecular-level dispersion in the PVA matrix would greatly improve the mechanical properties of the nanocomposites [65]. Therefore, the

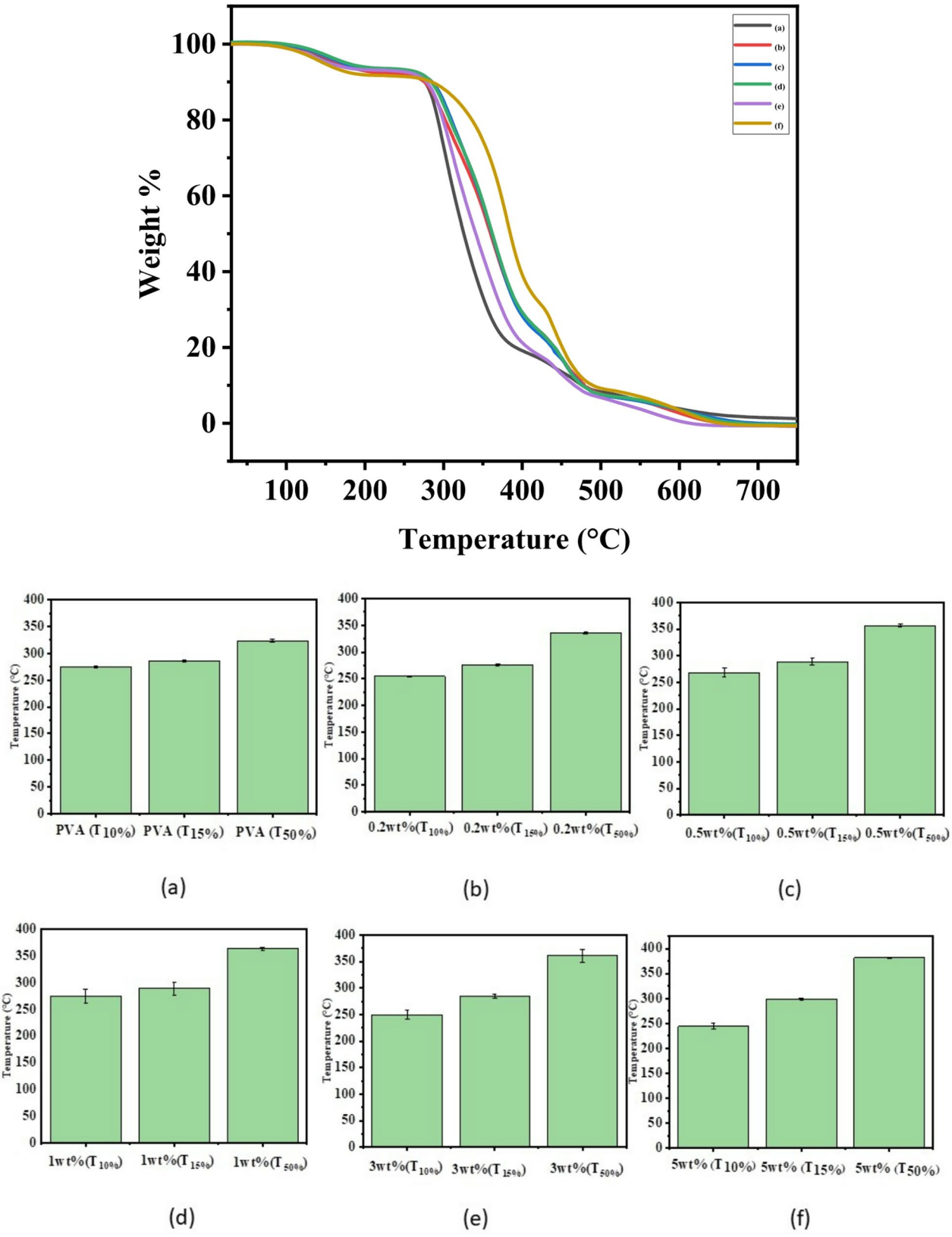

Fig. 10 TGA analysis and STDEV graph for (**a**) Pure PVA (**b**) 0.2% WBFB/PVA (**c**) 0.5% WBFB/PVA (**d**) 1.0% WBFB/PVA (**e**) 3.0% WBFB/PVA (**f**) 5.0% WBFB/PVA

Table 3 Thermal stability of WBFB/ PVA nanocomposites

Sample composition	$T_{10\%}$ (°C)	$T_{15\%}$ (°C)	$T_{50\%}$ (°C)
Pure PVA	276.17 ± 1.80	284.89 ± 1.25	325.70 ± 2.75
0.2wt% WBFB/PVA	275.44 ± 1.33	291.56 ± 1.81	359.71 ± 2.13
0.5wt% WBFB/PVA	285.28 ± 8.91	299.82 ± 6.46	361.43 ± 3.07
1.0wt% WBFB/PVA	284.24 ± 13.03	297.81 ± 12.12	361.97 ± 2.51
3.0wt% WBFB/PVA	278.27 ± 8.00	291.48 ± 4.36	340.85 ± 12.28
5.0wt% WBFB/PVA	284.89 ± 5.45	317.55 ± 2.55	384.81 ± 1.40

Table 4 DSC data for WBFB/PVA nanocomposites

Sample composition	T_m(°C)	T_c(°C)
Pure PVA	214.53	122.25
0.2wt% WBFB/PVA	218.84	123.13
0.5wt% WBFB/PVA	219.51	131.23
1.0wt% WBFB/PVA	220.46	132.63
3.0wt% WBFB/PVA	221.86	133.60
5.0wt% WBFB/PVA	223.32	135.27

mechanical performance of the polymer nanocomposites was enhanced by incorporating nano-level quantities of WBFB into a polymer matrix [66]. The standard stress-strain correlation for WBFB/PVA nanocomposites in the observed experimental variety of WBFB weight fractions is shown in Fig. 12. The findings indicate that the PVA matrix is reinforced by WBFB. Therefore, as the weight% of WBFB in the nanocomposites rises, the mechanical properties of the WBFB/PVA nanocomposites improve, particularly when compared to pure PVA polymer. Tensile strength increased from 43.851 MPa for PVA to 52.679 MPa for 0.2wt% WBFB/PVA a 20.13% increase 61.221 MPa for 0.5wt% WBFB/PVA a 39.61% increase 61.540 MPa for 1wt% WBFB/PVA a 40.33% increase 67.439 MPa for 3wt% WBFB/PVA a 53.79% increase and 71.228 MPa for 5wt% WBFB/PVA a 62.43% increase [12]. According to Table 5, these findings demonstrate a notable increase in the mechanical strength of WBFB/PVA nanocomposites at 5 wt% WBFB. This led to the development of a number of data-based conclusions. It is anticipated that the strong intermolecular interaction between the WBFB and the PVA structure a favorable aspect in the effective transfer of interfacial load from the polymer to the WBFB will result in improvements in the mechanical properties of the various nanocomposites each with a different WBFB wt% As a result, there is a strong non-covalent interfacial connection inside the PVA matrix between the oxygen-containing group of the WBFB and the hydroxyl group, most likely through an H-bonding interaction. According to FT-IR studies, this further improves the WBFB and PVA polymer matrix's homogeneous distribution. The young's modulus increase from 3088 MPa for Pure PVA to 7496 MPa for 5 wt% for WBFB/PVA as shown in Fig. 12. The elongation at break of pure PVA was 1.36%, and for 0.2, 0.5, 1, 3, and 5 wt% WBFB/PVA nanocomposites, it dropped to 1.35%, 0.94%, 0.91%, 0.92%, and 0.93%, respectively. As filler loading increases, this slow fall in fracture strain suggests a decline in ductility. The PVA chains' segmental mobility is restricted by the stiff WBFB particles, which

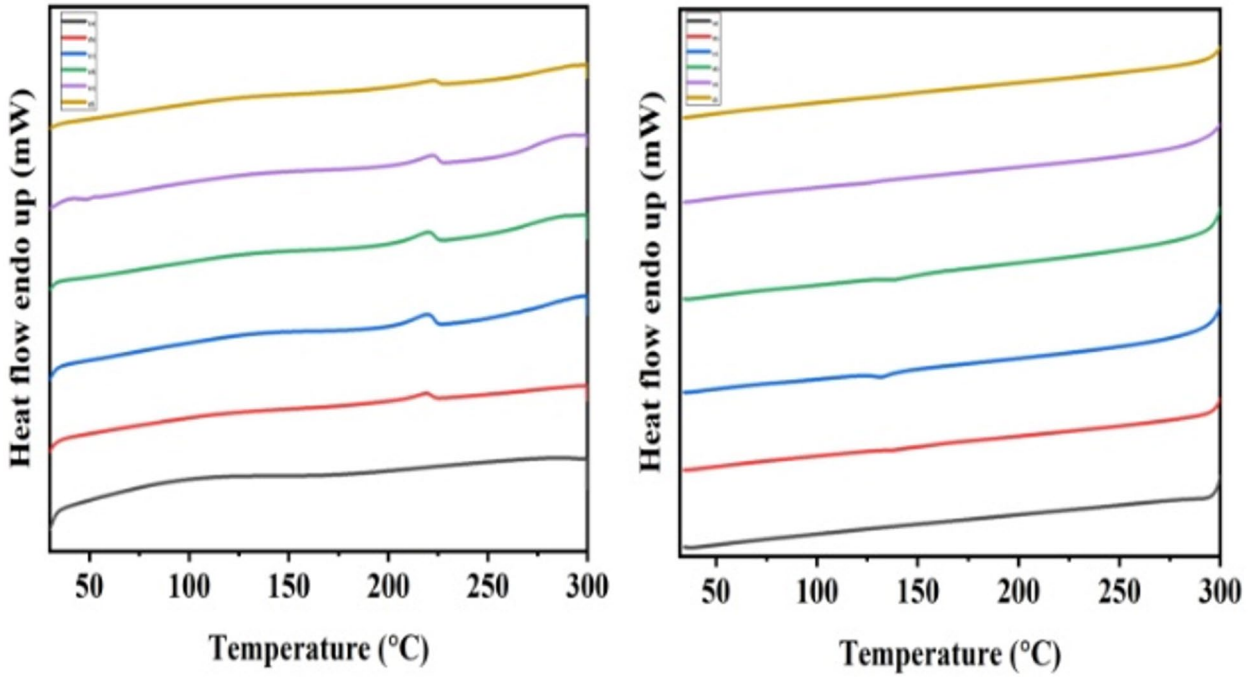

Fig. 11 DSC Heating and Cooling analysis of (**a**) Pure PVA (**b**) 0.2% WBFB/PVA (**c**) 0.5% WBFB/PVA (**d**) 1.0% WBFB/PVA (**e**) 3.0% WBFB/PVA (**f**) 5.0% WBFB/PVA

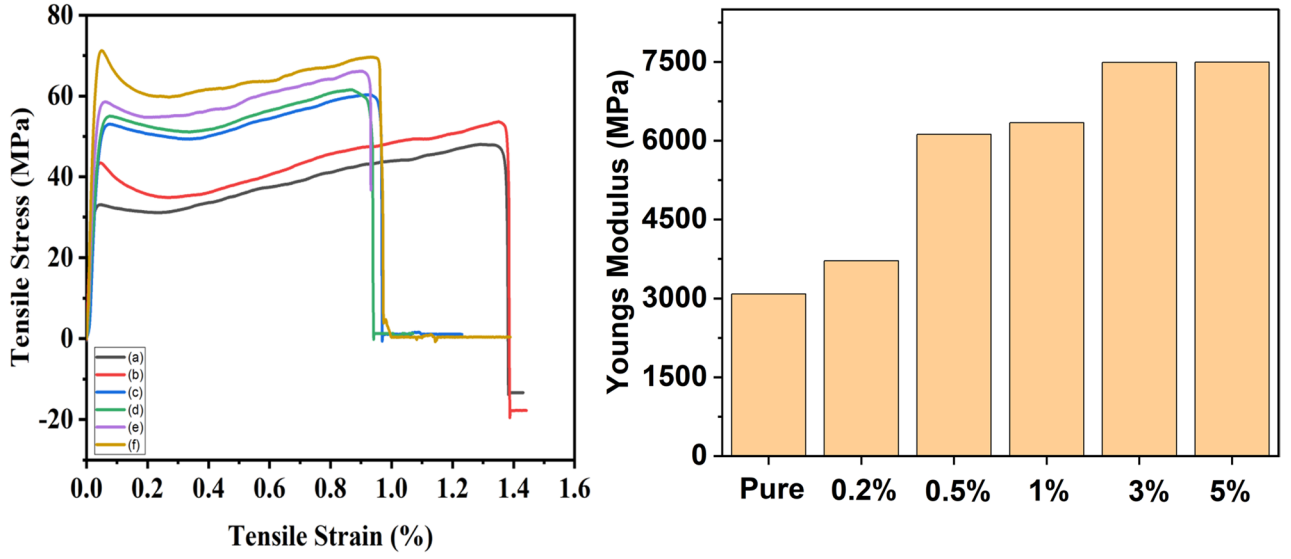

Fig. 12 Tensile strength and Young's modulus for (**a**) Pure PVA (**b**) 0.2% WBFB/PVA (**c**) 0.5% WBFB/PVA (**d**) 1.0% WBFB/PVA (**e**) 3.0% WBFB/PVA (**f**) 5.0% WBFB/PVA

Table 5 Tensile data for WBFB/PVA nanocomposites

Sample Composition	Tensile strength (MPa)	Increasing percentage	Youngs Modulus (MPa)	Toughness MJ/m³
Pure PVA	43.851 ± 13.36	-	3088	0.596
0.2wt% WBFB/PVA	52.679 ± 0.974	20.13%	3710	0.711
0.5wt% WBFB/PVA	61.221 ± 1.546	39.61%	6121	0.575
1.0wt% WBFB/PVA	61.540 ± 4.491	40.33%	6344	0.560
3.0wt% WBFB/PVA	67.439 ± 0.456	53.79%	7492	0.620
5.0wt% WBFB/PVA	71.228 ± 3.471	62.43%	7496	0.662

results in decreased deformability and early breakage under tensile strain. Toughness was 0.596 MJ/m³ for pure PVA and changed to 0.711, 0.575, 0.560, 0.620, and 0.662 MJ/m³ with increasing WBFB concentration, according to the area under the stress-strain curve. Along with a decrease in elongation at break, the concurrent increase in Young's modulus and tensile strength represents a common reinforcement-induced stiffening mechanism. WBFB and PVA have a strong non-covalent hydrogen bond that improves interfacial adhesion and load transfer efficiency but also reduces molecular flexibility. As a result, as the filler content increases, the nanocomposites' ductile behaviour changes to one that is more brittle.

Conclusion

The study reports that Bamboo stem (*Drepanostachyum falcatum*) serve as a tremendous precursor for the synthesis of biochar based materials. The pyrolysis method appears as the modest, cost effective attempt for the development of the high quality WBB. The confirmation of synthesized WBB and WBFB was examined with the help of RAMAN, FT-IR, XRD, TGA also morphological structure was studied by FE-SEM revealed the disordered surface like structure of WBB.

The PVA polymer matrix was further included with the synthesized WBFB using a straightforward solution mixing technique with varying weight percentages. Consequently, the WBFB and PVA matrix developed a homogeneous dispersion and H-bonding, greatly improving the PVA nanocomposite's mechanical and thermal characteristics. In addition to the great qualities of WBFB, we were able to convey the beneficial impacts of the WBFB/PVA nanocomposites. A 5 wt% addition of WBFB to the PVA matrix, tensile strength increased by approximately 62.43% compared to pure PVA and Young's modulus increased from 3088 MPa (pure PVA) to 7496 MPa, respectively. Thermal stability also increased from 325.70 °C ($T_{50\%}$) for pure PVA to 384.81 °C ($T_{50\%}$) for the 5% biochar functionalized composite. DSC analysis revealed enhanced in the thermal characteristics T_m and T_c by 8.79 °C and 13.02 °C. Furthermore, adding a substantial mechanical and thermal enhancement to composites with such little loading implies that matrix characteristics may be maintained for materials that are multifunctional biochar nanocomposite.

Acknowledgements
The authors would like to express their gratitude and appreciation to the Anusandhan National Research Foundation (ANRF), New Delhi (Ref. No. ANRF/PAIR/2025/000021/PAIR-A) and The National Research Council of Science and Technology (NST) grant from the government of Korea (MSIT) (CRC23013-000), and the Korea Institute of Science and Technology (KIST) Institutional Program.

Author contributions
Kunal Joshi: methodology, experiments, manuscript writing; Tanuja Arya: experiments, manuscript writing; Neelam Rawat: theoretical explanation; manuscript writing. Kundan Singh Rawat: review and editing. Chetna Tewari:

characterization; review and editing; Yong Chae Jung: review and editing; funding; Rajkumari Linthoinganbi: characterization; Pushpa Bhakuni Negi: review and editing; Nanda Gopal Sahoo: review and editing; supervision; funding.

Funding
Anusandhan National Research Foundation (ANRF), New Delhi (Ref. No. ANRF/PAIR/2025/000021/PAIR-A), National Research Council of Science and Technology (NST), Korea government (CRC23013-000), Republic of Korea, and the Korea Institute of Science and Technology (KIST) Institutional Program.

Data availability
The datasets generated and analysed during the current study are not publicly available due to the ongoing research project, but are available from the corresponding author upon reasonable request.

Declarations

Ethics approval and consent to participate
Not applicable.

Consent for publication
All authors read and approved the manuscript for publication.

Competing interests
The authors declare no competing interests.

Received: 31 December 2025 / Accepted: 6 March 2026
Published online: 30 March 2026

References

1. V. Ganesan, J.S. Chohan, A. Damodharan, P. Paramasivam, R. Maranan, High-performance biocomposites: leveraging lotus fiber and waste Kigelia pinnata fruit shell biochar for enhanced mechanical and fire-retardant properties. Polym. Bull. 1–35 (2025)
2. S. Kumar, C. Tewari, L. Philip, N.G. Sahoo, Enhanced physicochemical properties of Himalayan Weeping Bamboo-biochar for rapid multicomponent textile dyes uptake under classical and ultrasound irradiation: A comparative study. Next Sustain. **5**, 100089 (2025)
3. R.M. Karthik, L. Philip, Sorption of pharmaceutical compounds and nutrients by various porous low cost adsorbents. J. Environ. Chem. Eng. **9**(1), 104916 (2021)
4. N. Nippatla, L. Philip, Electrocoagulation-floatation assisted pulsed power plasma technology for the complete mineralization of potentially toxic dyes and real textile wastewater. Process Saf. Environ. Prot. **125**, 143–156 (2019)
5. P.B. Negi, M. Pathak, K.S. Rawat, N. Sahoo, A. Rana, C. Tewari, S. Biswas, Y.C. Jung, N.G. Sahoo, Green synthesis and machine learning driven analysis of SiO2 mixed carbon nanomaterial from agriwaste (rice husk) for supercapacitor applications. Mater. Chem. Phys. 131536 (2025)
6. B. Antil, S. Olhan, R.L. Vander Wal, Production of graphitic carbon from renewable lignocellulosic biomass source. Minerals **15**(3), 262 (2025)
7. M. Zubair, N.D. Mu'azu, N. Jarrah, N.I. Blaisi, H.A. Aziz, M.A. Al-Harthi, Adsorption behavior and mechanism of methylene blue, crystal violet, eriochrome black T, and methyl orange dyes onto biochar-derived date palm fronds waste produced at different pyrolysis conditions. Water Air Soil Pollut. **231**(5), 240 (2020)
8. C. Tewari, G. Tatrari, S. Kumar, S. Pandey, A. Rana, M. Pal, N.G. Sahoo, Green and cost-effective synthesis of 2D and 3D graphene-based nanomaterials from Drepanostachyum falcatum for bio-imaging and water purification applications. Chem. Eng. J. Adv. **10**, 100265 (2022)
9. F.I. Fajarwati, R. Hidayat, G. Fadillah, Synthesis and transformation of graphene-like structures from bamboo waste for photoelectrochemical devices. Carbon Trends **15**, 100351 (2024)
10. J. Huang, D. Li, L. Huang, S. Tan, T. Liu, Bio-based aerogel based on bamboo, waste paper, and reduced graphene oxide for oil/water separation. Langmuir. **38**(10), 3064–3075 (2022)
11. J. Ma, Y. Li, X. Yin, Y. Xu, J. Yue, J. Bao, T. Zhou, Poly (vinyl alcohol)/graphene oxide nanocomposites prepared by in situ polymerization with enhanced mechanical properties and water vapor barrier properties. RSC Adv. **6**(55), 49448–49458 (2016)
12. T. Arya, B.S. Bohra, C. Tewari, S. Dhali, V. Dikshit, S. Rana, Y.C. Jung, N.G. Sahoo, Influence of bio-resource-derived graphene oxide on the mechanical and thermal properties of poly (vinyl alcohol) nanocomposites. Polym. Compos. **45**(1), 695–708 (2024)
13. S. Olhan, B.K. Behera, Development of GNP nanofiller based textile structural composites for enhanced mechanical, thermal, and viscoelastic properties for automotive components. Adv. Compos. Hybrid. Mater. **7**(1), 25 (2024)
14. S. Olhan, B. Antil, B.K. Behera, Repair technologies for structural polymeric composites: An automotive perspective. Compos. Struct. **352**, 118711 (2025)
15. S. Olhan, B.K. Behera, Mechanical, thermogravimetric, and dynamic mechanical behavior of high-performance textile structural composite panels for automotive applications. J. Manuf. Process. **102**, 608–621 (2023)
16. M. Dinari, A. Haghighi, P. Asadi, Facile synthesis of ZnAl-EDTA layered double hydroxide/poly (vinyl alcohol) nanocomposites as an efficient adsorbent of Cd (II) ions from the aqueous solution. Appl. Clay Sci. **170**, 21–28 (2019)
17. S. Tripathi, G.K. Mehrotra, P.K. Dutta, Preparation and physicochemical evaluation of chitosan/poly (vinyl alcohol)/pectin ternary film for food-packaging applications. Carbohydr. Polym. **79**(3), 711–716 (2010)
18. M.M. Atta, E.O. Taha, A.M. Abdelreheem, Nitrogen plasma effect on the structural, thermal, and dynamic mechanical properties of PVA/starch/graphene oxide nanocomposite. Appl. Phys. A **127**(7), 532 (2021)
19. C. Tewari, Y.N. Kim, H. Muramatsu, M. Endo, Y.A. Kim, Y.C. Jung, Development and optimization of water-soluble double-walled carbon nanotubes by effective surface treatment of inner walls. Langmuir. **39**(19), 6698–6704 (2023)
20. C. Tewari, K.S. Rawat, Y. Kim, T. Arya, S. Dhali, S. Rana, D.V. Andreeva, B. Özyilmaz, R. Mahfouz, N. Qari, Y.C. Jung, Functional nanocarbons from waste plastics for energy storage applications. Renew. Sustain. Energy Rev. **226**, 116443 (2026)
21. N. Pandey, C. Tewari, S. Dhali, B.S. Bohra, S. Rana, S.P.S. Mehta, S. Singhal, A. Chaurasia, N.G. Sahoo, Effect of graphene oxide on the mechanical and thermal properties of graphene oxide/hytrelnanocomposites. J. Thermoplast. Compos. Mater. **34**(1), 55–67 (2021)
22. M. Pathak, G. Tatrari, M. Karakoti, S. Pandey, P.S. Sahu, B. Saha, N.G. Sahoo, Few layer graphenenanosheets from kinnow peel waste for high-performance supercapacitors: A comparative study with three different electrolytes. J. Energy Storage **55**, 105729 (2022)
23. G. Tatrari, C. Tewari, B.S. Bohra, S. Pandey, M. Karakoti, S. Kumar, H. Tiwari, S. Dhali, N.G. Sahoo, Waste plastic derived graphene sheets as nanofillersto enhance mechanical strength of concrete mixture: An inventive approach to deal with universal plastic waste. Clean. Eng. Technol. **5**, 100275 (2021)
24. M. Aboughaly, A. Babaei-Ghazvini, P. Dhar, R. Patel, B. Acharya, Enhancing the potential of polymer composites using biochar as a filler: a review. Polymers, **15**(19), 3981 (2023)
25. T. Kumar, S.A. Ansari, R. Sawarkar, A. Agashe, L. Singh, P.V. Nidheesh, Bamboo biochar: a multifunctional material for environmental sustainability. Biomass Conv. Bioref. 1–25 (2025)
26. E.F. Zama, B.J. Reid, H.P.H. Arp, G.X. Sun, H.Y. Yuan, Y.G. Zhu, Advances in research on the use of biochar in soil for remediation: a review. J. Soils Sediments. **18**(7), 2433–2450 (2018)
27. M. Mousa, Y. Dong, I.J. Davies, Eco-friendly polyvinyl alcohol (PVA)/bamboo charcoal (BC) nanocomposites with superior mechanical and thermal properties. Adv. Compos. Mater. **27**(5), 499–509 (2018)
28. H.K.F. Cheng, N.G. Sahoo, Y.P. Tan, Y. Pan, H. Bao, L. Li, S.H. Chan, J. Zhao, Poly (vinyl alcohol) nanocomposites filled with poly (vinyl alcohol)-grafted graphene oxide. ACS Appl. Mater. Interfaces. **4**(5), 2387–2394 (2012)
29. N. Nan, D.B. DeVallance, X. Xie, J. Wang, The effect of bio-carbon addition on the electrical, mechanical, and thermal properties of polyvinyl alcohol/biochar composites. J. Compos. Mater. **50**(9), 1161–1168 (2016)
30. S. Pandey, M. Karakoti, S. Dhali, N. Karki, B. SanthiBhushan, C. Tewari, S. Rana, A. Srivastava, A.B. Melkani, N.G. Sahoo, Bulk synthesis of graphene nanosheets from plastic waste: an invincible method of solid waste management for better tomorrow. Waste Manage. **88**, 48–55 (2019)
31. L. Jena, D. Soren, P.K. Deheri, P. Pattojoshi, Preparation, characterization and optical properties evaluations of bamboo charcoal. Curr. Res. Green. Sustainable Chem. **4**, 100077 (2021)
32. D. Pattnaik, S. Kumar, S.K. Bhuyan, S.C. Mishra, Effect of carbonization temperatures on biochar formation of bamboo leaves, IOP Conf. Ser. Mater. Sci. Eng. **338** (2018). https://doi.org/10.1088/1757-899X/338/1/012054

33. M.B. Mobarak, N.S. Pinky, S. Mustafi, F. Chowdhury, A. Nahar, U.S. Akhtar, M.S. Quddus, S. Yasmin, M.A. Alam, Unveiling the reactor effect: a comprehensive characterization of biochar derived from rubber seed shell via pyrolysis and in-house reactor. RSC Adv. **14**(41), 29848–29859 (2024)
34. H. Yang, J. Yang, L. Liu, B. Wang, Nano-biochar derived from bamboo biomass: A dual-functional material for electrochemical sensing of ferulic acid and adsorptive removal of surfactants in cosmetic wastewater. Int. J. Electrochem. Sci. **20**(4), 100959 (2025)
35. S.K. Das, G.K. Ghosh, R. Avasthe, K. Sinha, Morpho-mineralogical exploration of crop, weed and tree derived biochar. J. Hazard. Mater. **407**, 124370 (2021)
36. K. Krishnamoorthy, M. Veerapandian, K. Yun, S.J. Kim, The chemical and structural analysis of graphene oxide with different degrees of oxidation. Carbon. **53**, 38–49 (2013)
37. L.G. Pimenta Tienne, L.D.S. Candido, B.D.S. Macena da Cruz, F.F. Gondim, M.P. Ribeiro, R.A. Simao, M.D.F. Vieira Marques, S.N. Monteiro, Reduced graphene oxide synthesized by a new modified Hummer's method for enhancing thermal and crystallinity properties of Poly (vinylidene fluoride). J. Mater. Res. Technol. **18**, 4871 (2022)
38. L. Destiarti, R. Riyanto, R. Roto, M. Mudasir, Facile synthesis of reduced graphene oxide using Caesalpinia sappan L. extract as green reducing agent. Next Mater. **2**, 100134 (2024)
39. B. Lee, K. Li, H.S. Yoon, J. Yoon, Y. Mok, Y. Lee, H.H. Lee, Y.H. Kim, Membrane of functionalized reduced graphene oxide nanoplates with angstrom-level channels. Sci. Rep. **6**(1), 28052 (2016)
40. M.M. Storm, R.E. Johnsen, P. Norby, In situ X-ray powder diffraction studies of the synthesis of graphene oxide and formation of reduced graphene oxide. J. Solid State Chem. **240**, 49–54 (2016)
41. A. Cruz-Alcalde, N. López-Vinent, R.S. Ribeiro, J. Giménez, C. Sans, A.M. Silva, Persulfate activation by reduced graphene oxide membranes: Practical and mechanistic insights concerning organic pollutants abatement. Chem. Eng. J. **427**, 130994 (2022)
42. R.A.K. Hirani, A.H. Asif, N. Rafique, L. Shi, S. Zhang, M. Saunders, W. Tian, S. Wang, H. Sun, Heterogeneous activation of persulfate by macroscopic nitrogen-doped graphene oxide cubes for the degradation of antibiotic contaminants in water. Sep. Purif. Technol. **319**, 124110 (2023)
43. N. Rawat, S. Kathuria, S. Kumar, S. Nazir, P. Joshi, P.K. Singh, F.M. Hamzah, M. Diantoro, V.D. Punetha, P.S. Dhapola, Microporous activated carbon derived from Murraya Koenigii seeds for high-performance supercapacitors. Ionics 1–18 (2025)
44. C.C. Zhang, S. Hartlaub, I. Petrovic, B. Yilmaz, Raman spectroscopy characterization of amorphous coke generated in industrial processes. ACS omega. **7**(3), 2565–2570 (2022)
45. Y. Wang, D.C. Alsmeyer, R.L. McCreery, Raman spectroscopy of carbon materials: structural basis of observed spectra. Chem. Mater. **2**(5), 557–563 (1990)
46. R. Yuan, Y. Guo, I. Gurgan, N. Siddique, Y.S. Li, S. Jang, G.A. Noh, S.H. Kim, Raman spectroscopy analysis of disordered and amorphous carbon materials: a review of empirical correlations. Carbon 120214 (2025)
47. J. McDonald-Wharry, M. Manley-Harris, K. Pickering, Carbonisation of biomass-derived chars and the thermal reduction of a graphene oxide sample studied using Raman spectroscopy. Carbon. **59**, 383–405 (2013)
48. U. Muslima, M.U. Khandaker, S.M. Nawi, S.E. Lam, S.A. Sani, D.A. Bradley, M. Mahmoud, H.J. Woo, Thermoluminescence characterization of biochar material for dosimetric applications. Nucl. Eng. Technol. **57**(5), 103348 (2025)
49. R.Z. Amdani, F. Ossler, C. Brackmann, Raman spectroscopy for characterizing porous carbon. Laser Applications to Chemical, Security and Environmental Analysis (LTh4F–LTh43). Optica Publishing Group 2020 Jun
50. D. López-Díaz, M. Lopez Holgado, J.L. García-Fierro, M.M. Velázquez, Evolution of the Raman spectrum with the chemical composition of graphene oxide. J. Phys. Chem. C **121**(37), 20489–20497 (2017)
51. C.H. Chia, B. Gong, S.D. Joseph, C.E. Marjo, P. Munroe, A.M. Rich, Imaging of mineral-enriched biochar by FTIR, Raman and SEM–EDX. Vibr. Spectrosc. **62**, 248 (2012)
52. M. Li, P. Li, Q. Zhou, S.L.J. Lee, A mini review on persulfate activation by sustainable biochar for the removal of antibiotics. Materials **15**(17), 5832 (2022)
53. B. Xing, J. Dong, G. Yang, N. Jiang, X. Liu, J. Yuan, An insight into N, S-codoped activated carbon for the catalytic persulfate oxidation of organic pollutions in water: Effect of surface functionalization. Appl. Catal. A **602**, 117714 (2020)
54. X. Wang, K. Mao, J. Ma, H. Zhang, Y. Qian, H. Jin, K. Zhang, Balanced adsorption and catalysis in nitrogen-doped biochar for efficient peroxymonosulfate activation and 4-chlorophenol removal via electron transfer pathways. Appl. Surf. Sci. 164640 (2025)
55. M. Ilić, F.H. Haegel, A. Lolić, Z. Nedić, T. Tosti, I.S. Ignjatović, A. Linden, N.D. Jablonowski, H. Hartmann, Surface functional groups and degree of carbonization of selected chars from different processes and feedstock. PLoS One. **17**(11), e0277365 (2022)
56. D. Tang, L. Lu, Z. Luo, B. Yang, J. Ke, W. Lei, H. Zhen, Y. Zhuang, J. Sun, K. Chen, J. Sun, Heteroatom-doped hierarchically porous biochar for supercapacitor application and phenol pollutant remediation. Nanomaterials **12**(15), 2586 (2022)
57. Z. Cao, C. Yang, W. Zhang, H. Shao, Activated persulfate for efficient bisphenol A degradation via nitrogen-doped Fe/Mn bimetallic biochar. Water Sci. Technol. **90**(4), 1149–1163 (2024)
58. C. Zhang, H. Wu, F. Cheng, J. Li, Nonradical pathway transition from singlet oxygen to electron transfer in peroxydisulfate activation via regulation of nitrogen functional groups of biochar. J. Environ. Chem. Eng. 119502 (2025)
59. H.U. Rahim, E. Allevato, S.R. Stazi, Sulfur-functionalized biochar: Synthesis, characterization, and utilization for contaminated soil and water remediation-a review. J. Environ. Manage. **370**, 122670 (2024)
60. M. Zhao, Z. Xu, D.W. Tsang, Persulfate-based biochar-assisted advanced oxidation. Biochar Applications for Wastewater Treatment, pp. 213–227 (2023)
61. I. Tantis, G.C. Psarras, D. Tasis, Functionalized graphene–poly (vinyl alcohol) nanocomposites: Physical and dielectric properties. Express Polym. Lett. **6**(4), (2012)
62. J. Selvi, S. Mahalakshmi, V. Parthasarathy, C. Hu, Y.F. Lin, K.L. Tung, R. Anbarasan, A.A. Annie, Optical, thermal, mechanical properties, and non-isothermal degradation kinetic studies on PVA/CuOnanocomposites. Polym. Compos. **40**(9), 3737–3748 (2019)
63. S. Mallakpour, M. Dinari, Synthesis and properties of biodegradable poly (vinyl alcohol)/organo-nanoclaybionanocomposites. J. Polym. Environ. **20**(3), 732–740 (2012)
64. A. Bozdoğan, B. Aksakal, O. Yargi, Film formation and mechanical properties of an opaque titanium dioxide and transparent polyvinyl alcohol composite films. Polym. Compos. **41**(3), 939–950 (2020)
65. N.G. Sahoo, H.K.F. Cheng, L. Li, S.H. Chan, Z. Judeh, J. Zhao, Specific functionalization of carbon nanotubes for advanced polymer nanocomposites. Adv. Funct. Mater. **19**(24), 3962–3971 (2009)
66. B.S. Bohra, P. Singh, A. Rana, H. Sharma, T. Arya, M. Pathak, A. Chaurasia, S. Rana, N.G. Sahoo, Specific functionalized graphene oxide-based vitrimer epoxy nanocomposites for self-healing applications. Compos. Sci. Technol. **241**, 110143 (2023)

Publisher's note